GEOPHYSICS, VOL. 78, NO. 6 (NOVEMBER-DECEMBER 2013); P. KS97–KS105, 9 FIGS.
10.1190/GEO2013-0165.1

Long-period long-duration seismic events during hydraulic stimulation of shale and tight-gas reservoirs — Part 2: Location and mechanisms

Indrajit Das[1] and Mark D. Zoback[1]

ABSTRACT

Long-period long-duration (LPLD) seismic events that have been observed during hydraulic stimulation of shale-gas and tight-gas reservoirs appear to represent slow shear slip on relatively large faults. Within the limitations of the recording geometry, we determine the areas in the reservoirs where the events are located in two case studies in the Barnett shale. In one data set, LPLD events appear to occur in the region where the density of natural fractures as well as the fluid pressure during pumping were highest. In the other data set, the LPLD events are observed to occur between two wells and seem to establish a hydraulic connection between them. In both data sets, the LPLD events occur in areas with very few located microearthquakes. A combination of factors such as high fluid pressure and/or high clay content is potentially responsible for the slowly slipping faults. The LPLD events appear to be occurring only on faults large enough to produce a sequence of slow slip events. We suggest that these slowly slipping faults contribute appreciably to the stimulation of these extremely low-permeability reservoirs and hence mapping the distribution of faults and fractures and areas with rock properties that favor slow, sustained slip, can help in optimizing production.

INTRODUCTION

Das and Zoback (2013) show that long-period long-duration (LPLD) seismic events, recorded during hydraulic fracturing operations in the Barnett Shale, in the Horn River basin in Canada and in a Canadian tight-gas sand reservoir, appear to result from the superposition of numerous slow shear-slip events along relatively large faults. They also show that LPLD events are similar to tectonic tremors observed in subduction margins and transform boundaries, interpreted as swarms of low-frequency earthquakes (LFEs) (Ide et al., 2007; Shelly et al., 2007; Brown et al., 2009; La Rocca et al., 2009). They further demonstrate that seismic moment of large LPLD events is more than three orders of magnitude greater than $M_W \sim -2$ microearthquakes typically observed during multistage hydraulic fracturing stimulation. The characteristic 10–20-Hz corner frequencies of LPLD events (Das and Zoback, 2013) imply a fault dimension of at least 25–50 m, close to two orders of magnitude larger than those of microearthquakes (0.5–5 m). In the study area, the Barnett shale is about 100 m thick and the overall stimulation area of the wells is roughly 1000 m × 1000 m in one case (Barnett Data 1) and 500 × 1000 m in the other (Barnett Data 2). Therefore, the faults generating LPLD events are much larger than the faults associated with the microseismic events and relatively large with respect to the overall stimulated reservoir. These calculations indicate that LPLD events are potentially significant for permeability enhancement in these extremely low-permeability reservoirs. In this paper, we identify where these events are occurring in the reservoir and explain their mechanism in order to help maximize production from these reservoirs.

In earthquake seismology, several methods have been applied to accurately locate tremors and LFEs. Two of the methods which can potentially be modified and used to locate LPLD events are (1) the "source-scanning" method (Kao and Shan, 2004) in which the hypocenter is the location where the summed wave amplitudes at a network of stations are maximum and (2) the seismic-array method in which a tremor is located by triangulating the back-azimuths calculated from the apparent velocity measured at the surface arrays from the dominant signal in the 2–4-Hz band. (La Rocca et al., 2005, 2008). Location uncertainty is estimated to be on the order of 3–5 km (Rubinstein et al., 2010). The method most commonly used for locating tectonic tremors is envelope crosscorrelation, in which crosscorrelation is used to compute the delay between the envelopes of the tremor signal to determine the relative arrival times of the waves across a network of stations (Obara, 2002; Wech and Creager, 2008). However, the location uncertainty associated with

Manuscript received by the Editor 24 April 2013; revised manuscript received 2 July 2013; published online 17 October 2013.
[1]Stanford University, Geophysics Department, Palo Alto, California, USA. E-mail: idas@stanford.edu; zoback@stanford.edu.

envelope crosscorrelation is on the order of 20 km, and hence the method is not considered useful for locating LPLD events.

LOCATING LPLD EVENTS

There is significant difference between the recording geometry of tectonic tremors and that of LPLD events. Tectonic tremors are generally recorded by widely spaced (tens to hundreds of kilometers) surface broadband seismometers. LPLD events, on the other hand, are observed using downhole microseismic monitoring arrays with closely spaced geophones (~15 m) in each array. The latter is not ideal for LPLD event location because with a single or double array it is only possible to find the general direction of the LPLD events based on the direction and amount of the traveltime moveout. The low frequencies of the LPLD signals (~20 Hz) and the limited aperture of the monitoring arrays also makes it difficult to correct for the moveout and stack the data.

In the case of LPLD events recorded on a single array, we can estimate the angle of arrival of the LPLD events to the recording array from the moveout across the array. Although this indicates the general angular direction toward the event, there is no way to determine the azimuth in the plane orthogonal to the array, nor is there constraint on the distance of the events from the array, because there are no clear P- and S-wave arrivals. We try to solve this problem by choosing the most likely location based on where the hydraulic stimulation is occurring during that particular stage. Das and Zoback (2011) explain in detail how this method was applied in Barnett Data 1 (Figure 1a).

Barnett Data 1 consists of five horizontal wells (wells A, B, C, D, and E) hydraulically fractured in approximately 10 stages each (Das and Zoback, 2011). Wells A and B were fractured using a "simul-frac" method, whereas D and E were fractured using a "zipper-frac" method. They were monitored by a single recording array of nine 3C geophones in the central well C, which traversed the well once for the simul-frac and three times for the zipper-frac to keep it as close to the microearthquakes as possible. When well C was fractured, it was monitored by a single vertical array in the vertical portion of well B. Although the fluid and proppant volume pumped in each stage were similar, there was significant variation in the magnitude and number of microearthquakes and LPLD events detected in each stage. Stages 7 and 8 of the simul-frac produced the largest number of LPLD events and also the largest number of microearthquakes.

We crosscorrelated the entire filtered (10–80 Hz) LPLD waveforms in the first channel with the eight other channels to find the exact moveout across the array. The crosscorrelation gives the moveout amount with great accuracy (±1 ms). As the length of the array is known, the apparent velocity ($vel_{apparent}$) across the array is easily obtained. Using the relation

$$\text{Angle of arrival} = \cos^{-1}\left(\frac{vel_{formation}}{vel_{apparent}}\right) \qquad (1)$$

we can get the approximate angles of arrival because the formation velocity ($vel_{formation}$) is also known from well logs. The minimum and maximum S-wave velocity within the depth interval of the reservoir, based on sonic logs, are 2.0 and 2.4 km/s, respectively. The formation velocity ($vel_{formation}$) used in the above calculations is the average value of 2.2 km/s. Considering the uncertainty in

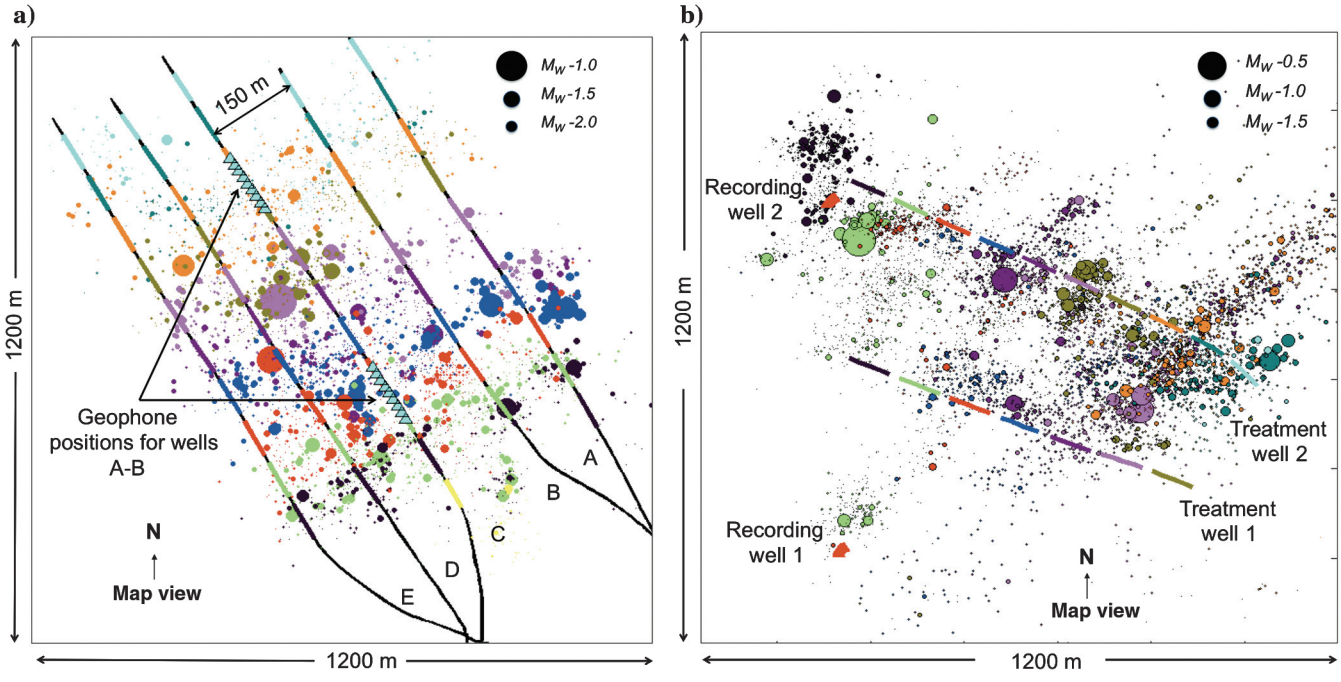

Figure 1. (a) Geometry and arrangement of wells A, B, C, D, and E in Barnett Data 1 along with all microearthquakes located by the microseismic vendor using traditional arrival time methods, shown colored according to stages and with sizes proportional to their magnitude. The locations of the nine 3C geophone arrays for monitoring stages 1–4 and stages 5–10, respectively, of wells A and B are shown as cyan triangles. (b) Geometry and arrangement of treatment wells 1 and 2 and recording wells 1 and 2 in Barnett Data 2, with all microearthquakes located by the vendor, again using traditional arrival time methods, shown as in (a).

S-wave velocity (±0.2 km/s) and the uncertainty in the moveout (±1 ms), the uncertainty of the angle of arrival is ±2°.

During the simul-frac and the zipper-frac, most LPLD events were produced by the later stage (stages marked in red in Figure 2). During treatment in well C, the first four stages (which followed the last stage of the zipper-frac without any significant time gap) and a few of the latter stages, produced LPLD events, all shown in green in the same figure. Interestingly, all LPLD events from the simul-frac and the zipper-frac appear to come from a narrow range of angles, 70°–100°. Red dotted lines show the two possible areas in the reservoir corresponding to this range of angles. All LPLD events in well C appear to come from the area enclosed within the green dotted lines. These are the projection of the cones formed by the maximum and minimum angles of arrival to the vertical recording array on the horizontal plane containing the wells. There is overlap between the two areas (red and green dotted lines) near stages 7 and 8 of the simul-frac, more precisely, near stage 8. Coupled with this is the fact that LPLD events were first recorded when stimulation was going on in stage 7 of the simul-frac. Also, as previously mentioned, stages 7 and 8 of the simul-frac produced by far the largest number of LPLD events. Based on these lines of evidence, it appears that the region near stage 8 of well A and B (yellow patch) is the most likely location where all the LPLD events are generated.

Upon further examination, we found that when we take smaller windows within each LPLD event instead of taking the whole event, certain windows give clear coherent peaks in the crosscorrelograms (Das and Zoback, 2011). These correspond to the low-frequency S-wave arrivals within the LPLD events (Das and Zoback, 2013) and come from the same range of angles, 70°–100°. One possible explanation is that each LPLD event results from the superposition of slow slip on adjacent sections of a large fault located within this range of angles.

Das and Zoback (2013) show that sometimes microearthquakes are also present within the LPLD events. Because of their small size, they are not reported by the microseismic vendor. We used the same basic method as described above to locate these microearthquakes. The logic is that a microearthquake, being a stronger signal than the low-frequency impulsive arrivals, will dictate the crosscorrelation in that particular window during an LPLD event. Figure 3b shows the results for corresponding LPLD events shown in Figure 3a from stage 7 of the simul-frac. The microearthquakes are plotted as blue stars, and the low-frequency arrivals as red dots. From Figure 3b we find that the microearthquakes that occurred within the LPLD events are constrained within the same narrow range of angles (70°–100°), suggesting that the microearthquakes might be related to slip on the same faults. In other words, the LPLD events and the microearthquakes might have a common source. Shown in Figure 3c are a few of the microearthquakes with clear P- and S-waves that we managed to locate from the moveout and S-P arrival time difference (Figure 4). The angle and the distance decrease with time for the three microearthquakes (i.e., they are moving from east to west), apparently along a fault with orientation similar to the dominant fracture orientation in neighboring well C, with a velocity of roughly 10 m/s (Figures 3c and 4).

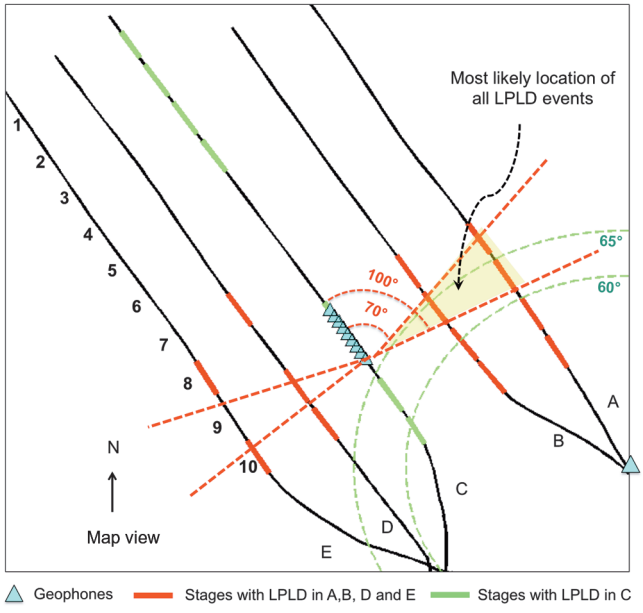

Figure 2. Most likely location of all LPLD events in the Barnett Data 1, shown in yellow. Stages producing LPLD events during the simul-frac and the zipper-frac are shown in red. Red dotted lines show their possible locations. Stages producing LPLD events in well C are shown in green. Area enclosed within green dotted circles shows their possible locations. The common area is chosen as the source of the LPLD events (see text).

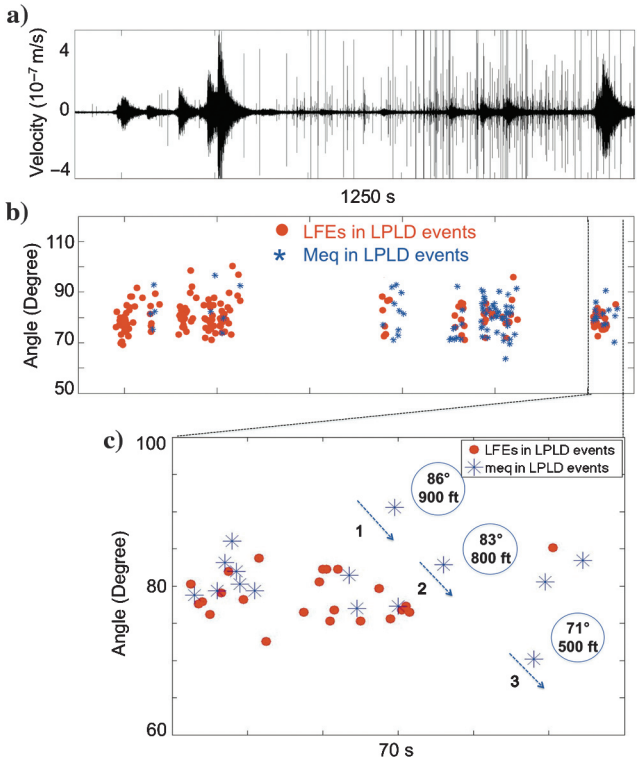

Figure 3. (a) Filtered waveform showing LPLD events observed during stage 7 of wells A and B in Barnett Data 1. (b) Plot of the angles of arrival of the low-frequency impulsive arrivals (red dots) and microearthquakes (blue stars) within each LPLD events. (c) A 60-second time period of the sequence shown in (b) at an expanded scale to highlight three microearthquakes within an LPLD event which could be located (Figure 4). The microearthquakes propagate at roughly 10 m/s during the event.

All the above observations are incorporated into a conceptual model for the generation of LPLD events (Figure 4), introduced in Das and Zoback (2011). According to this model, the sources of LPLD events are contiguous sections of relatively large preexisting natural faults in the reservoir. Such a hypothetical fault is shown in its most likely location (yellow patch, Figure 2) with orientation and position constrained by the fracture orientations seen in the adjacent well C and by the three located microearthquakes within an LPLD event (red stars) described above. The contiguous sections within this large fault, spanning the range of angles shown by the red dotted lines in Figure 2, are slowly slipping in close succession of each other. The signals from each individual failure superpose to create these long duration signals; in the process, they induce slip on small, local heterogeneities within the same fault zone, thereby generating microearthquakes. These microearthquakes are extremely small in size and mostly not detected during routine microseismic processing.

The range of angles associated with a single LPLD event (70°–100°) implies a fault dimension of about 100 m for a fault located in the area shown in yellow in Figure 4 with a strike of approximately N100°E. As the separation between the wells in Barnett Data 1 is ~150 m, a fault of this size, when activated, will significantly influence the stimulation process.

All microearthquakes reported by the microseismic vendor are also shown in Figure 4. The source of the LPLD events appears to be in a region with only a few located microearthquakes, an observation that we will encounter again in Barnett Data 2. Considering that stages 7 and 8 had the largest numbers and magnitudes of microearthquakes, it seems reasonable to consider this region void of microseismicity as real and not due to inaccurate event locations.

For Barnett Data 2 (Figure 1b), because we have two recording arrays, the source-scanning method of Kao and Shan (2004) can be applied, even though a minimum of three arrays would be considered an ideal recording geometry. This data set, discussed in Das and Zoback (2013), consists of two horizontal wells fractured in 8 and 10 stages, respectively. The hydraulic fracturing was recorded by vertical arrays in two different vertical wells, each with 40 three-component geophones. The geophones in both arrays were separated by 15 m such that each array is roughly 600-m long. The deepest geophones in recording wells 1 and 2 are ~450 m and 300 m above the two horizontal treatment wells, respectively. We take ~ 15-m (50-ft) resolution grids encompassing the entire stimulation volume and calculate the traveltimes to all the geophones from each grid, using the average S-wave velocity determined from sonic logs. We then take a filtered time window within an LPLD event with distinct, coherent S-wave arrivals and apply the traveltime corrections to all the traces and stack them. The grids corresponding to the highest power of stack are the most likely locations of the LPLD event. When the signal in both arrays are simultaneously traveltime corrected and stacked, we get two distinct cones of possible event locations in the 3D volume as shown in Figure 5. If we had three recording arrays, this ambiguity would not arise. One of the cones is located between the two simulation wells, while the other lies outside the area of stimulation. We find it reasonable to assume that the locations that lie within the area of active stimulation are the most likely source of the events. We have no constraint on the depth of the event, so we choose the event locations as ellipses defined by the plane of the wells intersecting the cone (Figure 5). Location ellipses corresponding to the large LPLD events recorded during various stages of stimulation in both wells (the first number within each ellipse refers to the treatment well and the second number to the

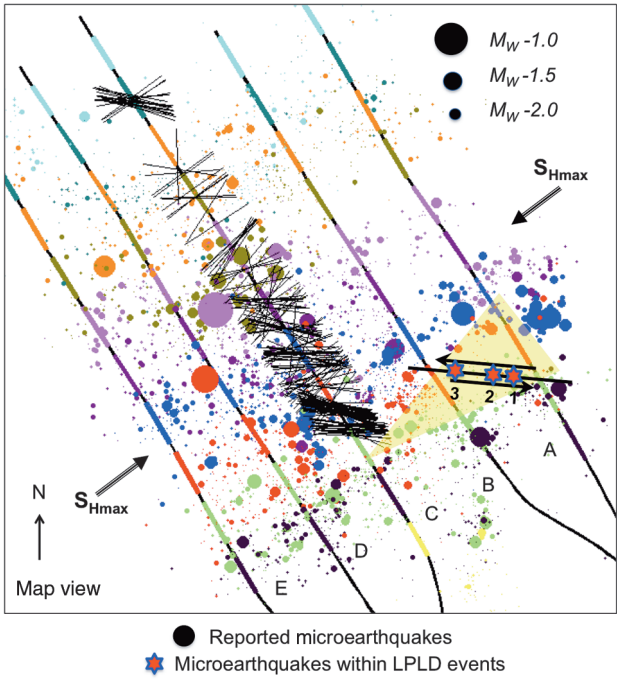

Figure 4. Conceptual model for the generation of LPLD events in Barnett Data 1. LPLD events are hypothesized to be associated with adjacent sections of large preexisting shear faults in their most likely locations shown in yellow (Figure 2). The orientation and position of this hypothetical fault is constrained by fracture orientations in adjacent well C (thin black lines) and the locations of three microearthquake within an LPLD event (Figure 3c) shown as red stars. The numbers below each show the order in which they occurred. The fault responsible for LPLD event lies in an area with only a few located microearthquakes.

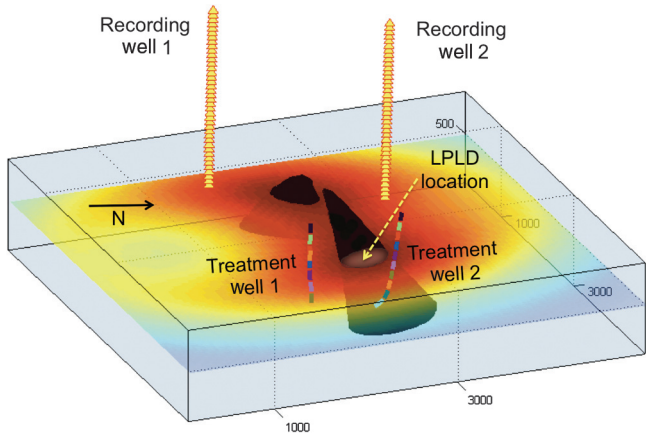

Figure 5. Two cones of possible locations of an LPLD event in Barnett Data 2 obtained by simultaneously correcting for traveltimes for signals recorded in both arrays and then stacking them (see text). The cone outside the area of stimulation is considered less likely to be the source of the LPLD events. There is no constraint on the depth with two arrays hence the depth of the treatment wells was selected as reasonable. The light-colored ellipse shows the intersection of the horizontal plane in the reservoir that contains the two wells, with the cone.

corresponding stage during which it was recorded) are shown in Figure 6 overlaid on a map of all microearthquakes located by the microseismic vendor. Note that all of the LPLD events are located in the same general area of the reservoir that spans the region between and near the centers of the two wells. In fact, stages near the heels and toes of the two wells also produce events that are located in this area even though the pressurization was going on more than 300-m away. Second, there is no systematic relation between the locations of events and the well that was being fractured when the event was recorded. For example, the event recorded during stage 3 of well 1 is located closer to well 2 and the event recorded during stage 6 of well 2 is located close to well 1. A fracture pathway between the two wells is thus indicated, and possibly a fluid connection as well, an inference supported by pressure recordings. During stimulation, it was noticed during the middle stages that the pressure increased in well 2 when pumping was going on in well 1 (and vice versa). It is also evident from Figure 6 that all the LPLD events are clustered in an area that has very few located microearthquakes.

Thus, from our observations in both Barnett data sets, it appears that LPLD events only occur in specific parts of the reservoir. In Barnett Data 1, all events occurred in the vicinity of two of the forty fracturing stages. In Barnett Data 2, all events were found clustered in the region between the wells, and in the vicinity of the central stages of both wells. In both data sets, however, the LPLD events appear to come from the region that is essentially devoid of microearthquakes. Note that here we are referring to the microearthquakes located by the vendor and not the microearthquakes identified within the LPLD events, which are extremely small in size and only detected using crosscorrelation. The latter are most likely due to slip on small heterogeneities along the slowly slipping large-scale faults responsible for generating LPLD events.

MECHANISM OF LPLD EVENTS

Owing to the characteristic similarity of LPLD events to tectonic tremors (Das and Zoback, 2011, 2013), we first discuss the current consensus on the mechanism of tectonic tremors to explore possible mechanism of LPLD events. Many lines of evidence — precise locations of tremors and LFEs on the plate interface in the transition zone between the locked and creeping sections of plate bounding faults (Ghosh et al., 2012), observed spatial and temporal correspondence between tremor and slow slip (Rogers and Dragert, 2003; Obara et al., 2004; Bartlow et al., 2011), P-wave focal mechanisms, and S-wave moment tensor inversions of stacked LFE waveforms showing slip in the plate convergence direction (Ide et al., 2007) — have together indicated that tremor is generated directly by shear slip on the plate interface and represents a seismic signature of the accompanying slow slip events. Previous authors (Nakata et al., 2008; Rubinstein et al., 2008; Thomas et al., 2009, 2012) have invoked extremely low effective normal stresses due to nearly lithostatic pore pressure when explaining the behavior of tectonic tremor. Hirose and Hirahara (2004) argue that spatial heterogeneity in frictional properties is necessary for slow slip to occur.

In the context of laboratory frictional experiments, Zoback et al. (2012) discussed the way in which the frictional parameter (a-b) varies with clay plus kerogen content in shale on samples. In brief, the frictional parameter (a-b) is diagnostic of frictional evolution with changes in sliding velocity. The term "a" refers to the instantaneous increase in friction that accompanies a step change in velocity. The parameter "b" describes how friction evolves with slip (Rice et al., 2001). Thus, (a-b) >0 describes a velocity-strengthening fault in which slow fault slip is expected because the fault gets stronger as sliding accelerates. Whereas (a-b) <0 describes a velocity-weakening material (one that produces earthquakes) in which fault gets weaker as sliding accelerates. Studying samples from various shale gas reservoirs, Kohli and Zoback (2013) found that shales with more than ~30% clay plus kerogen have frictional parameters (a-b) >0, implying stable sliding behavior or slow slip. Shales with clay plus kerogen content less than ~30% have (a-b) <0, implying unstable behavior, and most likely to produce microearthquakes.

Figure 7a and 7b show a correlation between the number of LPLD events and the instantaneous shut-in pressure (ISIP) values for the wells A and B in Barnett Data 1 (Das and Zoback, 2011). As shown in Vermylen and Zoback (2011), the ISIP increases stage by stage for all the wells as a poroelastic response to the injection, but the shorter time needed to complete all stages in the simul-frac, compared to the zipper-frac lead to the highest ISIP increase for wells A and B. Because this change in minimum horizontal stress (ΔS_h) is apparently a poroelastic response to the change in pore pressure (ΔP_p) in the reservoir, the change in ISIP is considered as a proxy for the minimum pore-pressure perturbation induced in the reservoir during the hydraulic fracturing experiment as ΔP_p must be greater than ΔS_h. Based on this, we generated a

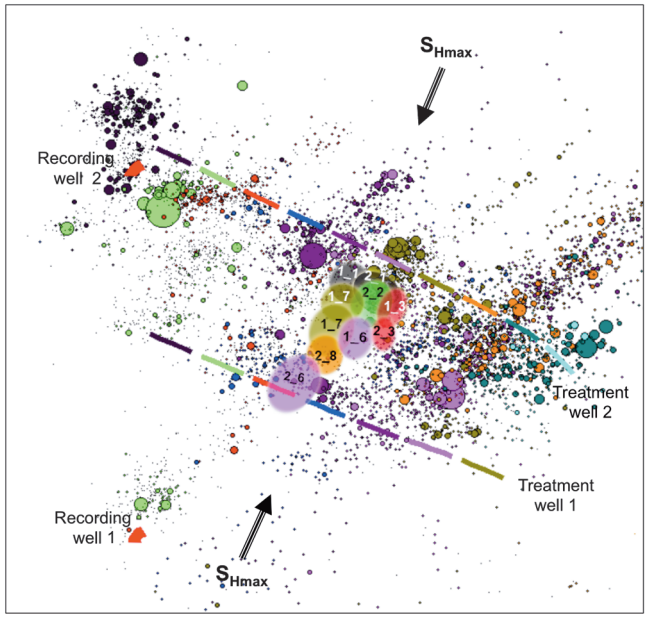

Figure 6. Location ellipses (see Figure 5) of large LPLD events recorded during various stages of both wells are overlaid on a map of the microseismic events recorded during the entire experiment. The ellipses are colored according to the active fracturing stages. The first number signifies the treatment well and the second number signifies the fracturing stage during which the event was recorded in. There appears to be a strong connection between the two wells with events related to treatment well 1 occurring near treatment well 2, and vice versa, and this is supported by pressure data from the company. Also clear is that all the LPLD events are located in a region with very few located microearthquakes, similar to observations in Barnett Data 1.

map of the minimum pressure perturbation experienced in the whole reservoir (Figure 7c). We found that the source area of the LPLD events (Figure 4) seems to coincide with the region of the largest pressure perturbation.

Slip behavior is also influenced by the orientation of a fault in the current stress field and by the fluid pressure. Zoback et al. (2012) demonstrated through modeling that slip induced by high fluid pressure on misoriented faults is expected to be slow, essentially because slip can occur only as rapidly as the fluid pressure propagates along the fault. Well-oriented faults, on the other hand, will slip catastrophically when triggered, to generate an earthquake.

Figure 8 illustrates how the faults and fractures parallel to those observed in the adjacent well C respond to this large pressure perturbation, using estimates of stress magnitudes developed by Vermylen and Zoback (2011). The stereo nets in Figure 8b show the poles to the preexisting fracture/fault in stages 6–9 of well C, in terms of the excess pressure needed to induce slip for a coefficient of friction of 0.6. We can see a wide variety of fracture and fault orientations. Figure 8a shows the condition at the initial reservoir pressure of 16 MPa. Only a few of the faults were close to being critically stressed (well-oriented), whereas most are poorly oriented in the current stress field prior to stimulation. A majority of them are far from the failure line and need high values of pore pressure to cause them to slip. We see in Figure 7c that pore-pressure perturbation was about 2 MPa throughout most of the reservoir affected by stimulation. As shown in Figure 8b, slip would be induced on a small number of well-oriented faults by such pressure changes. Figure 8c shows the effect of even higher pressures: A few of the poorly oriented faults are induced to slip. The maximum pressure change in the reservoir during stimulation was about 7 MPa, and that was in the region of stages 7 and 8 of wells A and B (Figure 7c). Figure 8d shows that, at this high pressure, many of the poorly oriented planes would be activated in shear. Slip would not have occurred on these faults in the in situ stress condition, but the extremely high pressure during pumping induces them to slip. For reasons discussed above, this induced slip on poorly oriented faults is expected to be slow. We believe that in Barnett Data 1 this is one of the conditions leading to the generation of LPLD events. This is supported by observations of the highest fracture density close to this region in adjacent well C (Figure 4) and a substantial negative seismic amplitude anomaly (interpreted to be due to an abundance of natural fractures) in the exact same area (Figure 9) and also the highest pore pressure perturbation observed in that region. Unfortunately for Barnett Data 2, neither fracture data nor ISIP data revealed any significant anomaly for any of the stages that would correlate with the LPLD event locations.

However, Figures 4 and 6 show that, in both data sets, the LPLD events seem to occur in the area of the reservoir that has very few located microearthquakes. We have discussed above that rocks with high clay content are generally expected to slip slowly and stably, whereas less clay-rich rocks are expected to slip unstably and generate microearthquakes. Because microearthquakes are virtually absent in the region where LPLD events occur, one possibility is that the formation rock in both cases has higher clay content near the source of the LPLD events.

In the case of Barnet data 2, the trend of the LPLD events is consistent with the dominant trend of the microearthquakes, which is 30° east of north. The stress direction determined from breakout analysis in treatment well 1 is 30° east of of north $\pm 20°$ which is identical to the stress direction (20° east of north) determined from breakouts and drilling-induced tensile fracture analysis in a nearby well (Sone, 2012). Because this is a normal faulting/strike slip environment and the trend of microearthquakes and LPLD events match the S_{Hmax} direction and orientation of natural fractures, we infer that both types of events evidently occur as a result of normal faulting on preexisting faults. The LPLD events, however, are generated by slow slip on the above faults, possibly because of higher clay content.

An alternative mechanism for generation of LPLD events might be fluid-induced oscillations of conduits transporting the injected hydraulic fracturing fluid. The similarity of volcanic tremor waveforms would seem to support the idea. However, as described in Das and Zoback (2013), LPLD event spectra are fundamentally different from volcanic tremor spectra and more similar to tectonic tremor spectra associated with slow fault slip. Fluid oscillations are expected to generate P-waves, whereas LPLD events have been observed to consist predominantly of S-waves and hence most likely due to shear slip on faults. In addition, LPLD events occur even before pumping starts in some stages (Das and Zoback, 2013) and continues even after pumping has stopped due to fluid pressure acting in the reservoir. From these lines of evidence, fluid oscillation in fractures does not appear to be a dominant mechanism for LPLD events.

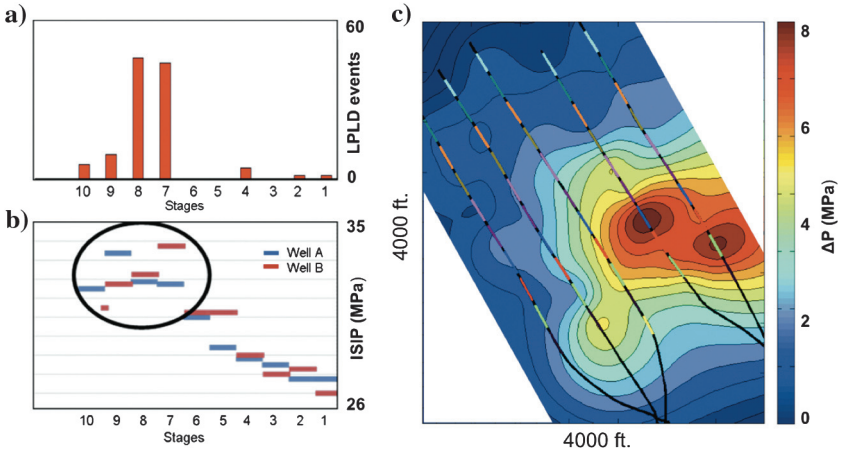

Figure 7. (a) LPLD events for all stages in wells A and B, plotted as red bars. (b) Instantaneous shut-in pressure (ISIP) for all stages (Vermylen and Zoback, 2011). (c) Estimate of the minimum pore-pressure perturbation that affected the reservoir during hydraulic fracturing of the five wells.

DISCUSSION

Das and Zoback (2013) calculate that the cumulative energy of LPLD events is one to two orders of magnitude higher than the cumulative energy of microearthquakes. Based on this, they conclude that LPLD events were potentially impacting the stimulation of gas reservoirs much more than microearthquakes. After modifying a few of the methods which earth scientists have successfully used to locate tremors on the subduction plate interface (Shelly et al., 2006; Brown et al., 2009; La Rocca et al., 2009; Ghosh et al., 2012; Ide, 2012), we were able

to approximately locate LPLD events observed in two Barnett data sets analyzed in detail.

We have demonstrated that LPLD events occur only in some specific parts of the reservoir, even when the wells are being pressurized in some other part. These observations are intriguing, but not unexpected, because Lacazette and Geiser (2013) have detected lateral communications through preexisting fracture systems over distances exceeding 1 km. They have also noticed activation of the said fracture networks approximately 1.5-km away from the treatment well within one hour of fracture initiation. We have also demonstrated that the sources of LPLD events are in the region of the reservoir with only a few located microearthquakes, possibly implying high clay content of the formation rocks there. In the case of Barnett Data 1, we have found that the most likely location of LPLD events appears to coincide with the region where the density of natural fractures is highest. We also have found highest pore pressure perturbation in the region where LPLD events occur in Barnett Data 1, and we theorize that shear slip on poorly oriented fractures caused

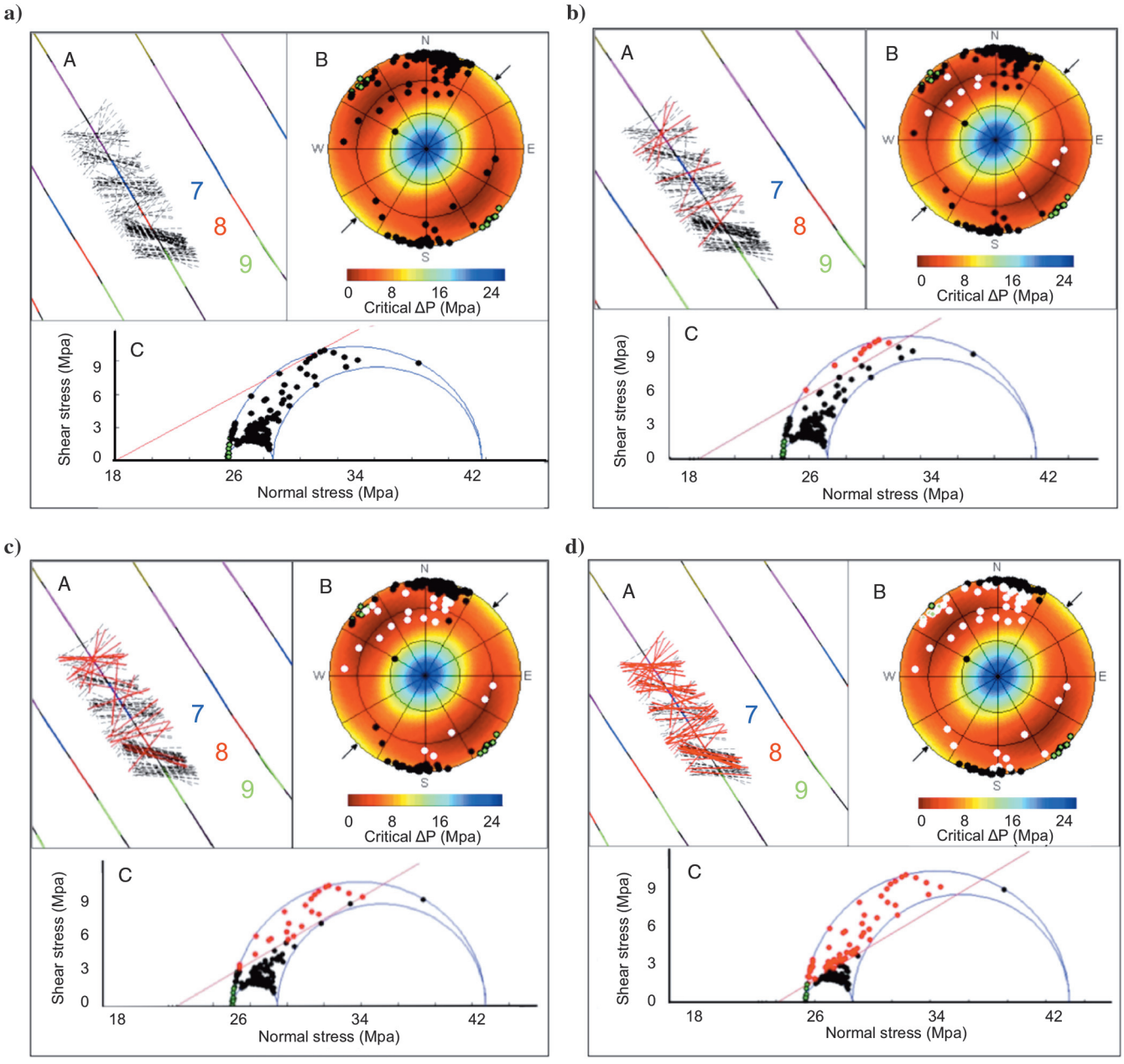

Figure 8. Stability analysis of fractures seen in stages 6–9 of well (c) in Barnett Data 1. (a) Shows the prestimulation scenario with no pressure perturbation; (b, c, and d) show the scenario for pressure perturbations of 2, 4, and 6 MPa, respectively. In the subfigures, panel A shows the number of activated natural fractures in red, B shows the stereonet with the activated fractures in white. The background color is the pressure necessary to initiate slip for a coefficient of friction of 0.6. Panel C shows the Mohr's circle representation of B. From (a–d), as the pore pressure is elevated, an increasing number of poorly oriented fractures is activated.

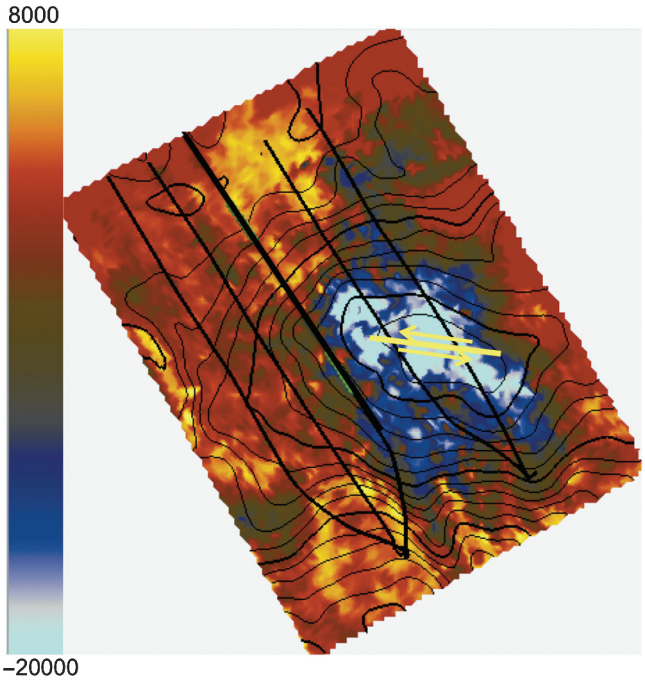

Figure 9. Seismic reflection amplitudes obtained from the 3D seismic data for the top of the formation of interest in Barnett Data 1. The numbers on the color scale represent the relative reflectivity of the Barnett shale. There is a large negative amplitude anomaly in the region of stages 7 and 8 of wells A and B, exactly in the region where all LPLD events originated. This low amplitude is interpreted to be due to an abundance of natural fractures. (The fracture set in Figure 4 is shown here in yellow.)

by the high fluid pressure during pumping might be one of the contributors to slow slip generating LPLD events.

If future studies are able to establish that these newly discovered events, evidently caused by pervasive slow slip on relatively large faults, are significantly impacting the stimulation of these extremely low permeability reservoirs, it might be possible to design reservoir stimulation in the most optimal and productive way by mapping the distribution of faults and fractures in areas with rock properties that favor slow sustained slip.

CONCLUSIONS

Despite the limitations of the recording geometries in the two Barnett data sets presented here, it is possible to approximately locate LPLD events. For Barnett Data 1, which was recorded by a single array, we used the back-azimuths obtained from the moveout across the array to constrain the angles of arrival. For Barnett Data 2, in which there were two arrays, it was possible to stack the traveltime corrected signal from grid blocks and the highest power of the stack gave us the likely locations for LPLD events.

In both data sets, we found that LPLD events occur only in specific parts of the reservoir and often occur regardless of which stage is being stimulated. These regions coincide with places that have very few microseismic events. Rocks with high clay content are expected to slip stably and slowly and may contain preexisting fractures and faults. There are many such pockets in the reservoir which are apparently unaffected by the stimulation in the context of conventional microseismicity, but it appears reasonable to speculate that there is a large number of slowly slipping faults in all those regions. However, LPLD events are only generated where faults large enough to produce a sequence of slow slip events exist. In Barnett Data 1 this argument is shown to be true as the region where LPLD events were located appears to be a portion of the reservoir with relatively large preexisting natural fractures, parts of which are slipping in close succession of each other to generate the LPLD events. Fluid pressure during pumping was also found to be the highest in this region. Slow slip on misoriented faults due to the high fluid pressure might be therefore another contributor to this phenomenon.

ACKNOWLEDGMENTS

We are grateful to ConocoPhillips Company for providing the data used in this research. We also thank Baker Hughes RDS for permission to use GMI•MohrFracs for the calculations shown in Figure 8 and Schlumberger for allowing us to use Petrel for generating Figure 9. We also wish to thank Pinnacle — a Halliburton service — for technical support. ConocoPhillips, Chevron, the Stanford Rock and Borehole Geophysics industrial affiliates program, and an SEG Foundation Scholarship provided funding for this research.

REFERENCES

Bartlow, N. M., S. Miyazaki, A. M. Bradley, and P. Segall, 2011, Space-time correlation of slip and tremor during the 2009 Cascadia slow slip event: Geophysical Research Letters, **38**, L18309, doi: 10.1029/2011GL048714.

Brown, J. R., G. C. Beroza, S. Ide, K. Ohta, D. R. Shelly, S. Y. Schwartz, W. Rabbel, M. Thorwart, and H. Kao, 2009, Deep low-frequency earthquakes in tremor localize to the plate interface in multiple subduction zones: Geophysical Research Letters, **36**, L19306, doi: 10.1029/2009GL040027.

Das, I., and M. D. Zoback, 2011, Long period long duration seismic events during hydraulic fracture stimulation of a shale gas reservoir: The Leading Edge, **30**, 778–786, doi: 10.1190/1.3609093.

Das, I., and M. D. Zoback, 2013, Long-period long-duration seismic events during hydraulic stimulation of shale and tight gas reservoirs — Part 1: Waveform characteristics: Geophysics, **78**, this issue, doi: 10.1190/GEO2013-0164.1.

Ghosh, A., J. E. Vidale, and K. C. Creager, 2012, Tremor asperities in the transition zone control evolution of slow earthquakes: Journal of Geophysical Research, **117**, B10301, doi: 10.1029/2012JB009249.

Hirose, H., and K. Hirahara, 2004, A 3-D quasi-static model for a variety of slip behavior on a subduction fault: Pure and Applied Geophysics, **161**, 2417–2431, doi: 10.1007/s00024-004-2573-7.

Ide, S., D. R. Shelly, and G. C. Beroza, 2007, Mechanism of deep low frequency earthquakes: Further evidence that deep non-volcanic tremor is generated by shear slip on the plate interface: Geophysical Research Letters, **34**, L03308, doi: 10.1029/2006GL028890.

Ide, S., 2012, Variety and spatial heterogeneity of tectonic tremor worldwide: Journal of Geophysical Research, **117**, B03302, doi: 10.1029/2011JB008840.

Kao, H., and S. Shan, 2004, The source-scanning algorithm: Mapping the distribution of seismic sources in time and space: Geophysical Journal International, **157**, 589–594, doi: 10.1111/j.1365-246X.2004.02276.x.

Kohli, A. H., and M. D. Zoback, 2013, Frictional properties of shale reservoir rocks: Journal of Geophysical Research: Solid Earth, **118**, doi: 10.1002/jgrb.50346.

Lacazette, A., and P. Geiser, 2013, Comment on Davies et al., 2012 — Hydraulic fractures: How far can they go?: Marine and Petroleum Geology, **43**, 516–518, doi: 10.1016/j.marpetgeo.2012.12.008.

La Rocca, M., K. C. Creager, D. Galluzzo, S. Malone, J. E. Vidale, J. R. Sweet, and A. G. Wech, 2009, Cascadia tremor located near plate interface constrained by S minus P wave times: Science, **323**, 620–623, doi: 10.1126/science.1167112.

La Rocca, M., D. Galluzzo, S. Malone, W. McCausland, G. Saccorotti, and E. D. Pezzo, 2008, Testing small-aperture array analysis on well-located earthquakes, and application to the location of deep tremor: Bulletin of the Seismological Society of America, **98**, 620–635, doi: 10.1785/0120060185.

La Rocca, M., W. McCausland, D. Galluzzo, S. Malone, G. Saccorotti, and E. D. Pezzo, 2005, Array measurements of deep tremor signals in the

Cascadia subduction zone: Geophysical Research Letters, **32**, L21319, doi: 10.1029/2005GL023974.
Nakata, R., N. Suda, and H. Tsuruoka, 2008, Non-volcanic tremor resulting from the combined effect of Earth tides and slow slip events: Nature Geoscience, **1**, 676–678, doi: 10.1038/ngeo288.
Obara, K., 2002, Nonvolcanic deep tremor associated with subduction in southwest Japan: Science, **296**, 1679–1681, doi: 10.1126/science.1070378.
Obara, K., H. Hirose, F. Yamamizu, and K. Kasahara, 2004, Episodic slow slip events accompanied by non-volcanic tremors in southwest Japan subduction zone: Geophysical Research Letters, **31**, L23602, doi: 10.1029/2004GL020848.
Rice, J. R., N. Lapusta, and K. Ranjith, 2001, Rate and state dependent friction and the stability of sliding between elastically deformable solids: Journal of the Mechanics and Physics of Solids, **49**, 1865–1898, doi: 10.1016/S0022-5096(01)00042-4.
Rogers, G., and H. Dragert, 2003, Episodic tremor and slip on the Cascadia subduction zone: The chatter of silent slip: Science, **300**, 1942–1943, doi: 10.1126/science.1084783.
Rubinstein, J. L., M. L. Rocca, J. E. Vidale, K. C. Creager, and A. G. Wech, 2008, Tidal modulation of nonvolcanic tremor: Science, **319**, 186–189, doi: 10.1126/science.1150558.
Rubinstein, J. L., D. R. Shelly, and W. L. Ellsworth, 2010, Non-volcanic tremor: A window into the roots of fault zones: New Frontiers in Integrated Solid Earth Sciences, 287–314, doi: 10.1007/978-90-481-2737-5_8.
Shelly, D. R., G. C. Beroza, and S. Ide, 2007, Non-volcanic tremor and low-frequency earthquake swarms: Nature, **446**, 305–307, doi: 10.1038/nature05666.
Shelly, D. R., G. C. Beroza, S. Ide, and S. Nakamuta, 2006, Low-frequency earthquakes in Shikoku, japan, and their relationship to episodic tremor and slip: Nature, **442**, 188–191, doi: 10.1038/nature04931.
Sone, H., 2012, Mechanical properties of shale gas reservoir rocks and its relation to the in-situ stress variation observed in shale gas reservoirs: Ph.D. thesis, Stanford University.
Thomas, A. M., R. Bürgmann, D. R. Shelly, N. M. Beeler, and M. L. Rudolph, 2012, Tidal triggering of low frequency earthquakes near Parkfield, California: Implications for fault mechanics within the brittle-ductile transition: Journal of Geophysical Research, **117**, B05301, doi: 10.1029/2011JB009036.
Thomas, A. M., R. M. Nadeau, and R. Bürgmann, 2009, Tremor-tide correlations and near-lithostatic pore pressure on the deep San Andreas fault: Nature, **462**, 1048–1051, doi: 10.1038/nature08654.
Vermylen, J. P., and M. D. Zoback, 2011, Hydraulic fracturing, microseismic magnitudes, and stress evolution in the Barnett Shale, Texas, USA: SPE, 140507.
Wech, A. G., and K. C. Creager, 2008, Automated detection and location of Cascadia tremor: Geophysical Research Letters, **35**, L20302, doi: 10.1029/2008GL035458.
Zoback, M. D., A. Kohli, I. Das, and M. McClure, 2012, The importance of slow slip on faults during hydraulic fracturing stimulation of shale gas reservoirs: SPE, 155476.